Atomization and Sprays, 29(7):629–654 (2019)

DECOUPLING THE EFFECT OF SURFACE TENSION AND VISCOSITY ON SPRAY CHARACTERISTICS UNDER DIFFERENT AMBIENT PRESSURES: NEAR-NOZZLE BEHAVIOR AND MACROSCOPIC CHARACTERISTICS

Zehao Feng,[1,2] Shangqing Tong,[1] Chenglong Tang,[1,*] Cheng Zhan,[1] Keiya Nishida,[2] & Zuohua Huang[1]

[1]*State Key Laboratory of Multiphase Flow in Power Engineering, Xi'an Jiaotong University, Xi'an, 710049, People's Republic of China*

[2]*Department of Mechanical System Engineering, University of Hiroshima, 1-4-1, Kagamiyama, Higashi-Hiroshima 739-8527, Japan*

*Address all correspondence to: Chenglong Tang, State Key Laboratory of Multiphase Flow in Power Engineering, Xi'an Jiaotong University, Xi'an, 710049, People's Republic of China, E-mail: chenglongtang@mail.xjtu.edu.cn

Original Manuscript Submitted: 5/7/2019; Final Draft Received: 11/28/2019

This work experimentally investigates the effect of the surface tension and viscosity on the spray characteristics at low (1 atm) and high (10 and 20 atm) ambient pressures. The surface tension and viscosity of the liquids vary from 26.41 to 60.93 mN/m and 1.01 to 7.45 mPa · s, respectively. First, by using the long focus distance microscope and the pulse laser illumination at the near-nozzle region, high spatial resolution initial spray morphology was captured to explore the effect of surface tension and viscosity on the primary breakup behavior. Results show that less ligaments and droplets were detected with the increase of surface tension. Increasing viscosity for fixed surface tension delays the breakup and consequently postpones the formation of spray ligaments and droplets. The near-nozzle spray morphology is more sensitive to the variation of viscosity, compared to the surface tension. Second, high-speed photography is utilized to record the macroscopic spray behaviors. The results show that, at high ambient pressures, with the increase of surface tension or the viscosity, the spray tip penetration becomes longer and the spray cone angle becomes smaller. In addition, the spray cone angle is more sensitive to the change of the surface tension than viscosity. However, at low ambient pressure, both the surface tension and viscosity show weak influence. Finally, the classic Hiroyasu model for spray tip penetration was extended to accommodate liquids with varying surface tension and viscosity. The modified correlation matches the experimental data well, and the spray tip penetration is more sensitive to the variation of the surface tension, compared to the viscosity.

KEY WORDS: *surface tension, viscosity, spray, near-nozzle behavior, macroscopic spray characteristics*

1. INTRODUCTION

The pollutant emissions of a diesel engine, particularly the soot and NOx, depend strongly on the control of mixture formation with a high-pressure injection system. In order to improve diesel engine performance, optimization of the diesel spray and mixture formation, aided by in-cylinder 3D computational fluid dynamics, becomes increasingly important (Kowalski, 2017).

Another widely recognized approach to reduce emissions of a diesel engine is to substitute fossil diesel with alternative fuels, particularly biodiesel, ethanol, and other oxygenated hydrocarbons. Many researchers have investigated the spray and atomization characteristics of alternative fuels with or without the presence of diesel (Bohl et al., 2017; Wang et al., 2010). Li et al. (2017) experimentally studied the spray characteristics of long-chain alcohol-diesel blends (n-butanol or n-pentanol) in a constant volume chamber. They found that the blends show a shorter spray tip penetration (STP), and a larger spray cone angle (SCA) and spray projected area compared with pure diesel. The effect of ethanol and di-ethyl ether addition on the spray characteristics of diesel/biodiesel blends has been investigated by Zhan et al. (2018) under high injection pressure. The results showed that with the addition of ethanol and diethyl ether (DEE), the STP decreases and the corresponding projected area increases greatly because of the decreased viscosity and surface tension. Furthermore, they found that the Sauter mean diameter (SMD) is decreased when ethanol and DEE blended, and DEE addition most favors the atomization process. The macroscopic spray characteristics of four next-generation biofuels—hydrotreated vegetable oil (HVO), palm oil methyl ester (PME), soybean oil methyl ester (SME), and used cooking oil methyl ester (UCOME)—were investigated in detail by Bohl et al. (2017) using a constant-volume spray vessel, which is compared with the reference mineral diesel. The results show that HVO with the lowest density presents the shortest STP distance and the largest SCA, resulting in a more distributed fuel-air mixture. In recent years, many mathematical models of macroscopic spray characteristics were developed and tested by using both mineral diesel and alternative fuels at various conditions (Agarwal et al., 2014; Desantes et al., 2017; Mohan et al., 2017; Yu et al., 2016, 2017).

According to these investigations, the physical properties including the surface tension, viscosity, vapor pressure, and density of the liquid fuel frequently affect the spray and atomization characteristics such as STP, SCA, mass flow rate, droplet size, and velocity after breakup. In fact, according to Chung and Presser (2001), fuel with higher viscosity delays atomization by suppressing the instabilities required for the primary breakup of the fuel jet, and higher fuel surface tension opposes the formation of small droplets from the liquid fuel. Experimental studies (Chung and Presser, 2001; Ramamurthi et al., 1998) also demonstrated that increasing the surface tension or the viscosity of the liquid inhibits the growth of surface waves and generates more deformed liquid sheets. Surface tension and viscosity are the most direct acting factors and are regarded as the essential reasons for the primary and secondary breakup processes of the spray (Bohl et al., 2017; Chung and Presser, 2001; Desantes et al., 2009). Primary breakup occurs at or near the nozzle exit where bulk fluid, typically in the form of a sheet or jet, breaks up for the first time and forms the ligaments and big droplets. Secondary atomization occurs further downstream, as the ligaments and big droplets break up into small droplets (Shinjo and Umemura, 2010; Tang et al., 2017b).

The surface tension and viscosity are independent physical properties of any alternative fuel. Their effect on the spray has not been decoupled because in most of the previous work, selecting different liquid changes the surface tension, and viscosity changes accordingly. Few experimental results have answered the question, which is the most sensitive physical property for the spray

characteristics, the liquid surface tension or the viscosity? Davanlou et al. (2015) conducted an experimental study on the breakup regimes, including droplet coalescence of liquids with different viscosity and surface tension from a hollow cone hydraulic injector nozzle. The viscosity and the surface tension of these liquids can be changed separately by adding different amounts of glycerol or surfactant into water. The results demonstrated that liquids with lower surface tension decrease the average droplet diameter and increase the probability of coalescence between droplet collisions. In addition, an increase in viscosity leads to higher average drop sizes that are induced by primary and secondary breakup. An experimental study that focused on the effects of liquid viscosity on the spray characteristics and instability during the transient operation of a swirl atomizer was conducted by Yao et al. (2012). Water–glycerol mixtures were used to change the liquid viscosity with the surface tension being constant. They found that the fluid viscosity plays a critical role in controlling the liquid sheet breakup and atomization. Ellis et al. (2001) investigated the surface tension effect on characteristics of the spray produced by a hydraulic nozzle using surfactant solutions, which can fix the viscosity. Different liquid sheet morphology and smaller spray drop sizes were found with the increase of surfactant concentration.

The main objective of this paper is to understand the individual effects of surface tension and viscosity on spray primary breakup and macroscopic spray characteristics using a diesel injector. It is very useful to characterize alternative fuel sprays. First, spray morphology of the liquids with different surface tension and viscosity were visualized at varying ambient pressures by using a high time and spatial resolution particle/droplet imaging analysis (PDIA). The primary breakup mechanism will be emphatically discussed, especially the effect of ambient pressure, viscosity, and surface tension. At the same time, the spray tip velocity of these liquids at different phases was obtained by using the double-frame, double-exposure technique. Second, the spray macroscopic data such as the STP and the SCA from varying surface tensions and viscosities will be characterized. In addition, correlations to accommodate the viscosity and surface tension effect for the STP will be provided for the new experimental data based on the existing classical correlation given by Hiroyasu and Arai (1990).

2. EXPERIMENTAL SETUP AND PROCEDURE

2.1 Tested Liquids

In the experiments, a different quantity of surfactant was added into the distilled water to alter the surface tension. The surfactant was injected using a microsyringe, and the mixture was stirred to ensure perfect mixing. After that, the whole injection system, including the pipeline and the injector, was cleaned by the prepared liquid at least five times. The surface tension of the mixture was measured by a JYW-200 automatic interface tension meter with an accuracy of 0.1 mN/m. Glycerol was used to alter the viscosity with limited change in density. The dynamic viscosity is measured by an NDJ-1 rotary viscometer with less than 5% uncertainty. The surface tension, dynamic viscosity, and density of tested fuels at 24.5°C were measured under Chinese National Standards GB/T 6541-1986, GB/T 265-1988, and GB/T 1884-1992, respectively. The measured physical properties of the liquids used in experiments are presented in Table 1. It is seen from Table 1 that the liquids S1–S4 have almost constant viscosity and density while the surface tension changes significantly. The liquids V1–V5 have almost constant surface tension and density while the viscosity varies significantly. The effect of the viscosity and surface tension on the spray characteristics will then be compared.

TABLE 1: Liquids properties at 24.5°C

Liquids	S1	S2	S3	S4	V1	V2	V3	V4	V5
Surface tension (mN/m), σ	26.41	36.75	48.92	60.93	61.23	61.25	61.31	61.37	61.45
Viscosity (mPa · s), μ	1.02	1.02	1.01	1.01	1.01	1.38	2.38	4.15	7.45
Density (kg/m^3), ρ	999	999	998	998	998	1008	1025	1050	1095

2.2 Experimental Apparatus and Procedure

A schematic diagram of the experimental apparatus for the spray macroscopic evolution measurement is shown in Fig. 1. The system consists of four parts: a high-pressure injection system, a constant volume vessel, an optical imaging system, and a synchronization circuit. The high-pressure injection system consists of a fuel tank to store liquid, a hand pump with a filter, a high-pressure common rail, and a single-hole diesel injector with a nozzle diameter of 0.2 mm. The high-pressure common rail is used as a pressure stabilizing and cooling chamber. The pressure sensor is mounted on the common rail to monitor injection pressure. The injection pressure P_{inj} is maintained at 400 bar during the whole experiment.

The liquid is injected into a constant volume vessel filled with nitrogen to produce different ambient pressure conditions. Three ambient pressures, P_{amb} = 1, 10, and 20 bar, were tested. Three quartz windows with diameter of 100 mm and thickness of 60 mm are installed on the sides of the vessel to allow for optical access. A Xeon lamp (100 W) is used as the light source for a high-speed camera (Phantom V611) with a sampling frequency of 20,000 fps, a spatial resolution set as 384 × 600 pixels^2, and an exposure time of 20 μs.

For the PDIA system for near-nozzle microscopic imaging, the original optical imaging system was replaced as shown in Fig. 2. The PDIA system delivers a visual impression of the spray structure that allows for detecting liquid fragments of any shape and gives good insight into the breakup process (Sallevelt et al., 2015). A double-pulsed Nd:YAG laser serves as the light source for the measurements. The laser emits light with a wavelength of 532 nm, a pulse duration of 5 ns, and a maximum pulse energy of 220 mJ. The pulses are short enough to avoid any motion blur to obtain images of high resolution. A ground glass diffuser with a dye plate is placed just in front of the laser to obtain a uniform illumination of the image background. The images were

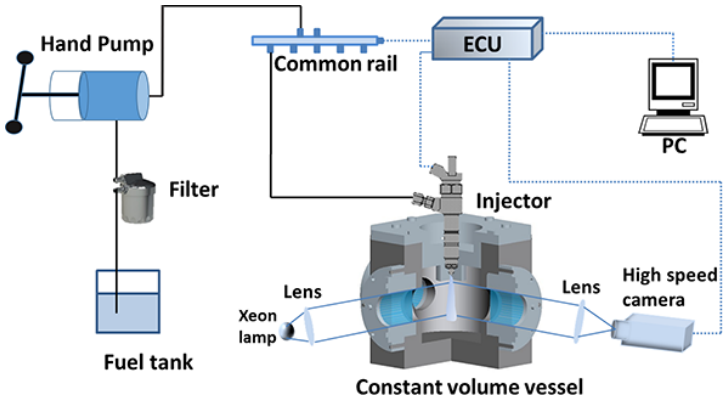

FIG. 1: Schematic diagram of macroscopic spray evolution imaging

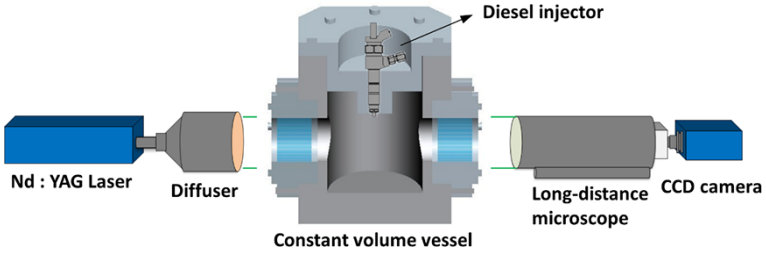

FIG. 2: Schematic diagram of microscopic imaging optical path

captured using a charge-coupled device (CCD) camera (ImagerProSX 5M) with a resolution of 2456 $\times$ 2058 pixels^2. The camera lens is replaced by a long-distance microscope, the working distance of which varies from 56 to 152 cm. In this investigation, the focal distance was set as 61 cm, and the field of view was 1866 $\times$ 1563 μm^2 after calibration, providing a high resolution ratio of 1.316 pixel/μm. In this experiment, the position of the light source is fixed, while the CCD camera and microscope position can be adjusted electronically by a three-way positioner MC600 with a displacement accuracy of 1 μm to shift the focal point toward the desired location in the spray. When capturing the near-nozzle spray, the target window of the CCD camera is adjusted to the location where the nozzle tip just appeared at the top of the measurement window.

The synchronization circuit mainly consists of a remote electronic controller OD2301 from Beijing PowerMac Corporation with a closed loop control, and a programmable time unit (PTU). The injection width (1.5 ms) and rail pressure were set and monitored by OD2301. Laser and camera systems are synchronized using the PTU by the signal delay control system. Figure 3 shows pulse sequences of different trigger signals for near-nozzle spray characteristics investigation. The laser signal delay is to synchronize the mechanism of injector and laser beam, which controls the precise time of fuel advent at the nozzle exit. By adjusting laser delay time (T), which has an accuracy of 1 μs, near-nozzle sprays at different phases were captured.

3. RESULTS AND DISCUSSION

3.1 Near-Nozzle Spray Characteristics

The primary breakup that dominates the spray initiation evolution is of great importance for the spray and combustion process (Wang et al., 2016a). Better knowledge of primary breakup will

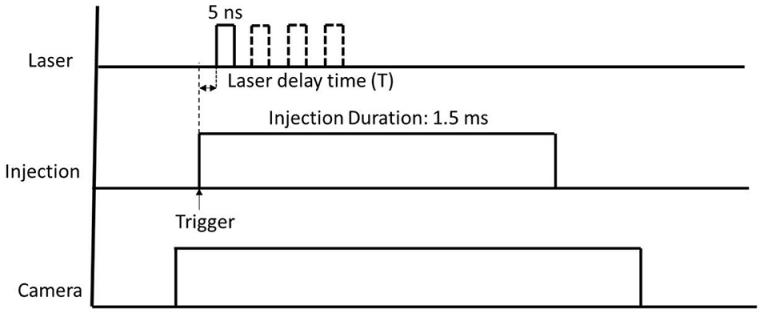

FIG. 3: Time sequence control of microscopic characteristics measurement

lead to better predictions of spray characteristics such as the initial jet structure, spray angle, and droplet size distribution, and thus this is strongly needed. For primary breakup, the events usually occur at a very near-nozzle field within a few millimeters downstream of the injector tip and are mainly affected by aerodynamics, cavitation, and turbulence generated inside the nozzle (Som and Aggarwal, 2010). In this section, we will discuss the influence of the ambient pressure, liquid surface tension, and viscosity on the very near-nozzle spray morphology and tip velocity through the analysis of the high-resolution images.

3.1.1 Effect of Ambient Pressure

Figure 4 shows the typical spray images at the immediate near-nozzle region (0 $\sim$ 3.5 mm) for V1 liquid at three ambient pressures. In the early stage ($T = 10$ μs) of the near-nozzle jet, the surface instability waves are visually confirmed for all the ambient pressures. It can be seen that from the nozzle tip the main jet develops from a smooth liquid column to a side-waved one. It is indicated that the surface wave is generated at the jet tip because of the gas–liquid interaction. This wave then propagates along the liquid core toward upstream, as shown by the top rectangle. This is consistent with the numerical results of Shinjo and Umemura (2010), which pointed out that two paths (one is through gas phase and the other through droplet impact) of disturbance transmission toward upstream exist. It is also observed that there are many thread-like ligaments created from the crest of the surface wave as shown in the middle rectangle at $P_{amb} = 10$ and 20 bar. This breakup resulted from the unstable waves growing at the liquid surface (Som and Aggarwal, 2010), which is one of the most important aerodynamic mechanisms. The surface flow velocity is lower than the inner flow; the crests exposed to the air are more easily sheared

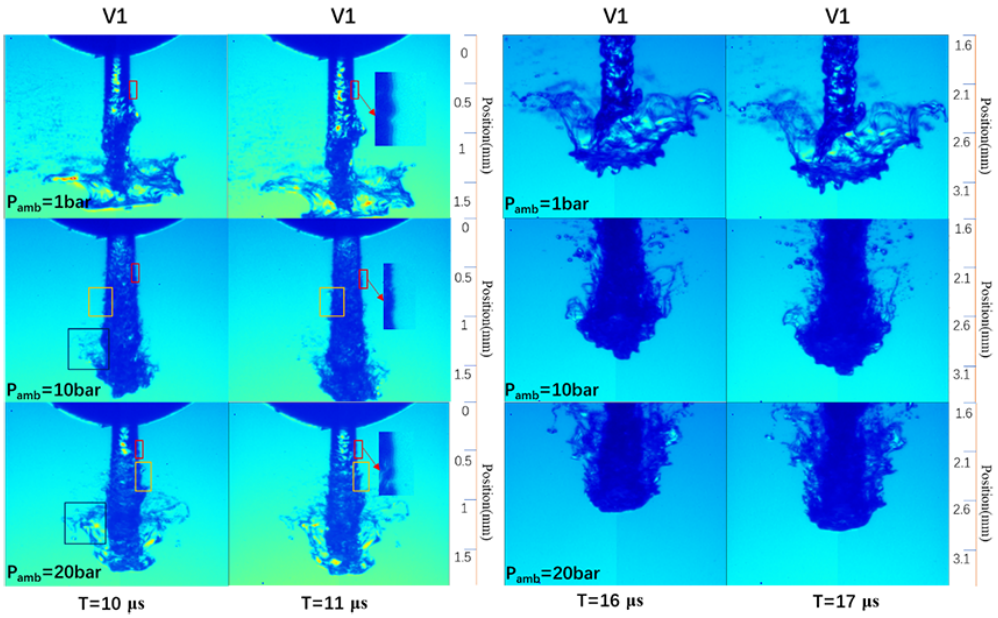

FIG. 4: Comparison of spray microscopic morphology at near-nozzle region between different ambient pressures

by the aerodynamic force. When the shear stress exceeds the surface tension force, the crest breakup and ligaments will be formed.

Many complex responses may occur at spray tip because it is the region where the interaction between liquid and ambient air first happens. The most typical structure is the "mushroom" that has been reported in many previous works (Wang et al., 2016a,b; Wei et al., 2017). These works indicate that the mushroom-shaped head forms usually 1 or 2 microseconds after the liquid jet appears out of the nozzle. The mushroom-shape tip evolves and is enlarged toward the radial expansion, and strong vortices are formed behind this mushroom shape, as the numerical results revealed (Shinjo and Umemura, 2010). Under the force of the shear stress and air friction, the liquid film at the edge of the tip becomes thinner, surface wave oscillation magnitude increases, and the sheet begins to expand and finally break up into small ligaments as shown by the region marked in black rectangles. These experimental observations at $P_{amb} = 10$ and 20 bar have manifested the aerodynamic mechanism proposed by numerical simulation in Shinjo and Umemura (2010).

However, very different structures are found at low ambient pressure ($P_{amb} = 1$ bar). The tip suffers from severe disturbance and the liquid film is expanded to the radial direction at a very high speed. Many small droplets are found in the region very far away from the main jet. And more, an unsocial protuberance is present at the side of the liquid column. Obviously, this deformation is not induced by the aerodynamic force but seemingly by the burst pressure. We suspect that this structure collapse is caused by the air bubbles formed inside the nozzle, also called cavitation. At the exit, the compressed air bubbles are catastrophically collapsed, pushing the breakup of the jet and movement of small droplets. This indicates that the divergence of the bubble breakup energy formed by cavitation induces fine primary breakup. The propensity of nozzle cavitation is usually quantified by the cavitation number (K) in previous research (Suh and Lee, 2008; Wei et al., 2017), defined as

$$K = \frac{P_{\text{inj}} - P_v}{(1/2)\rho_l u^2} \tag{1}$$

where P_v represents the liquid saturation pressure, ρ_l is the liquid density, and u is the liquid jet velocity. For lower ambient pressure, the velocity of the fluid in the nozzle increases, as shown in Fig. 5, and the cavitation is more likely to occur; this is the reason for the observed bubble bursting like structures as shown by the 1 atm case in Fig. 4.

At $T = 16$ μs, with high disruptive shearing forces acting on the liquid, rough surface columns consisting of branched and elongated liquid fragments are formed at $P_{amb} = 10$ and 20 bar. Also, solely large spray drops with an almost spherical shape are pinched off from branches and ligaments. In addition, some gas entrainment is detected at the jet periphery. This is because, as the spray tip penetrates, more and more of its momentum is transformed to the turbulent intensity of the surrounding charge, as discussed by Moon et al. (2014). It is found that more vigorous entrainment occurs at $P_{amb} = 20$ bar, indicating better primary breakup. At $P_{amb} = 1$ bar, the collapsed spray tip continues to evolve and a wide and thin sheet of liquid film is formed. However, the aerodynamic effect is found very weak under atmospheric pressure. Thus, at two sides of the liquid column, no branched structure is observed. The results imply that in the near-nozzle region cavitation has a dramatic but short-lived effect on breakup and is more noteworthy at low ambient pressure, while the aerodynamics has a long-term effect and the effect is more significant at high ambient pressure. We note that both cases will promote primary breakup.

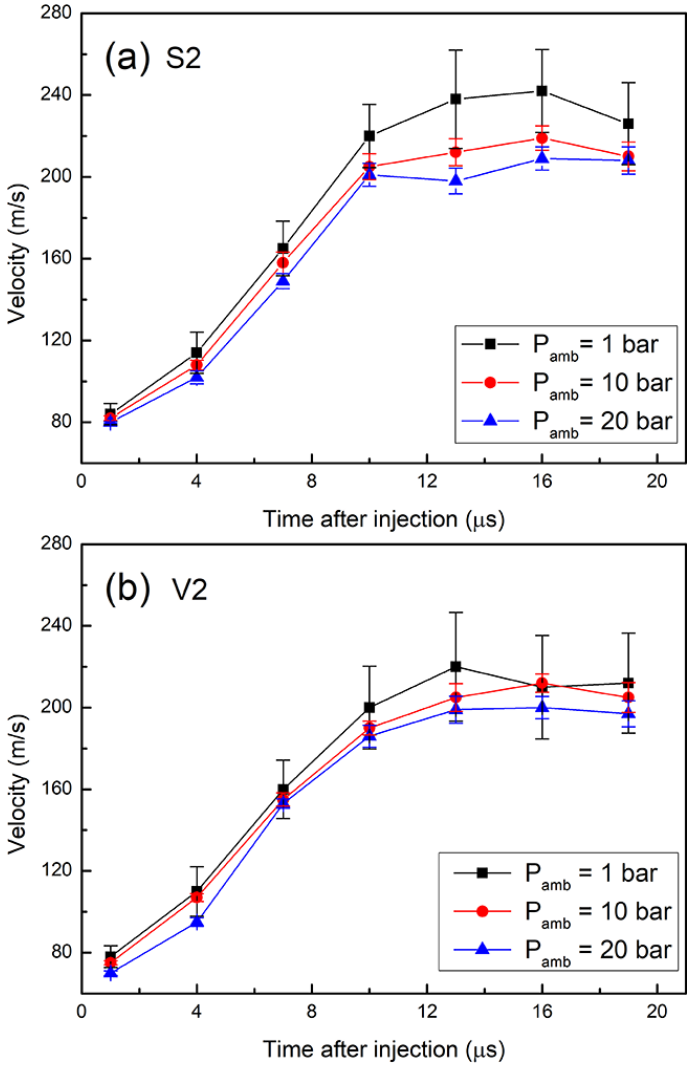

FIG. 5: Effect of ambient pressure on near-nozzle spray tip velocity

The near-nozzle spray tip velocity at different ambient pressures for liquids S2 and V2 were plotted as a function of time, as shown in Fig. 5. The velocity is determined by counting the tip displacement in the two frames during the delay time (1 μs) of the two laser pulses. Five repeated experiments have been conducted and the error bars in Fig. 5 represent the standard deviation. It is found that the standard deviation at $P_{amb} = 1$ bar are bigger than that of the other two conditions. This is because of the unstable spray structure caused by the catastrophic bubble bursting as discussed above. For all three ambient pressure conditions, the tip velocity evolves in a very similar pattern: initially after injection, the velocity increases almost linearly with time, and then show an almost constant value with some fluctuations. We note that this does not mean that the velocity will always maintain this constant value because of the transient nature of the spray in this study.

3.1.2 Effect of Surface Tension

For low ambient pressure condition ($P_{amb} = 1$ bar), cavitation is favored as discussed in the preceding section, and the bubbles that are formed by cavitation burst into ligaments or droplets, as shown by the images in the first row for S1 and S2 in Fig. 6(a). With the increase of liquid surface tension, the liquid sheet-like structures are observed, as shown by the images in the first row for S3 and S4 in Fig. 6(a). This is because, with the increase of surface tension, the enhanced interfacial force of the bubble makes its bursting more difficult and the liquid-sheet-like structure that expands is then observed. In a slight downstream region, as shown by the second row images in Fig. 6(a), bubble bursting is already finished and increasing surface tension shows weak influence on the spray tip morphology. The spray tip velocity at this low ambient pressure shows also very weak influence of the surface tension, as shown in Fig. 7(a).

For higher ambient pressure cases ($P_{amb} = 20$ bar) as shown in Fig. 6(b), with the increasing surface tension, slightly less ligaments and droplets are observed at the periphery of the jet. This is because the increased surface tension leads to an increased resistance force for droplets to be

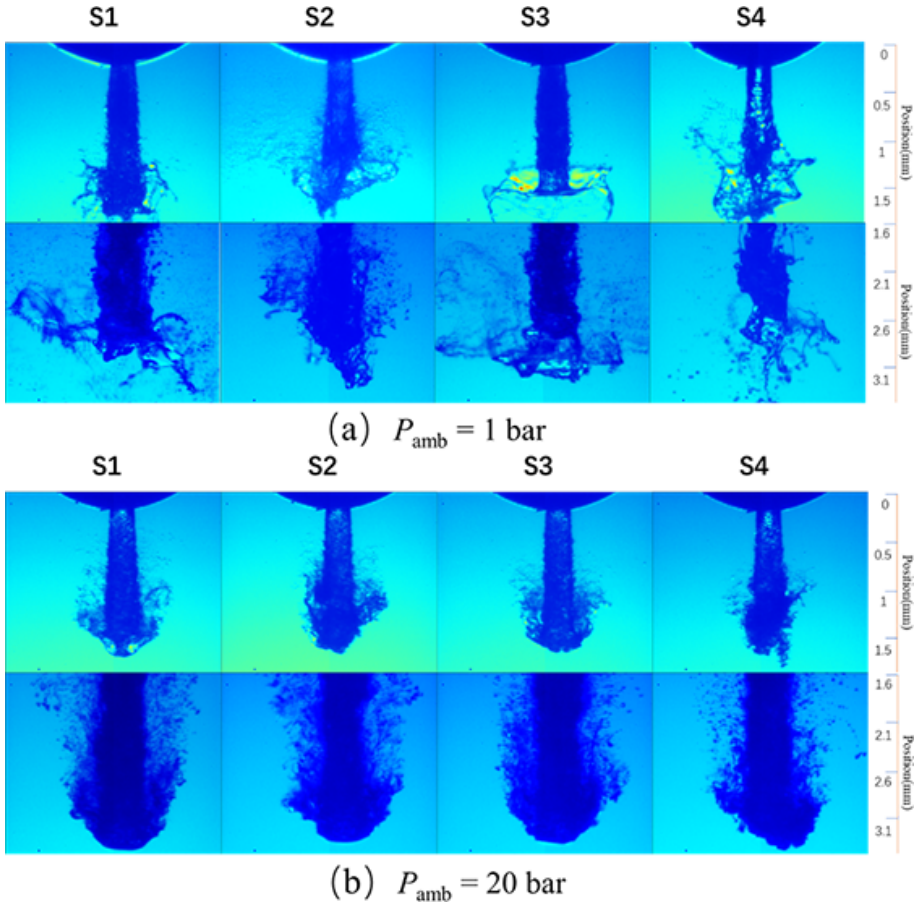

FIG. 6: Comparison of spray microscopic morphology at near-nozzle region between different surface tension liquids

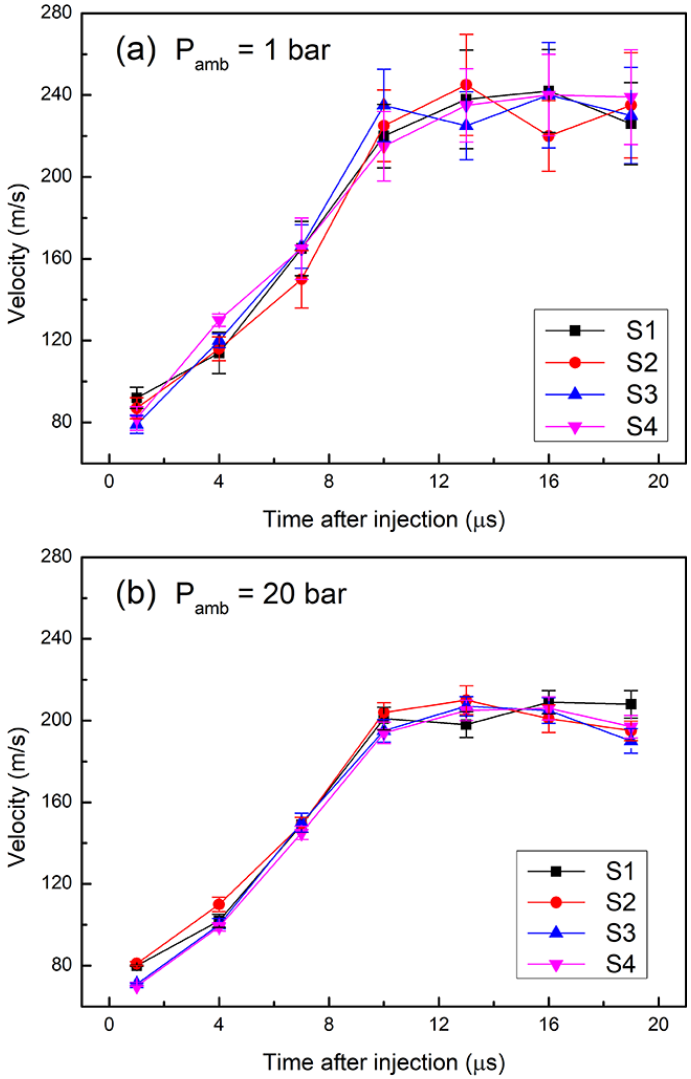

FIG. 7: Effect of surface tension on near-nozzle spray tip velocity

formed along the surface of the liquid jet. The spray tip velocity for this ambient pressure also shows no influence of the surface tension, as in Fig. 7(b). Similar to the low ambient pressure case, at this ambient pressure, the tip velocity for all the liquids with varying surface tension first increases to a stable value of around 200 m/s after around 10 μs.

3.1.3 Effect of Viscosity

The near-nozzle spray images for different viscosity liquids are shown in Fig. 8. For relatively smaller viscosity liquids at $P_{amb} = 1$ bar, surface waves and liquid sheet-like breakup were also found, as shown by the images for liquids V1 to V3 in Fig. 8(a). However, for more viscous liquids (V4 and V5), no more liquid sheet-like structures were observed. The effect of the viscosity

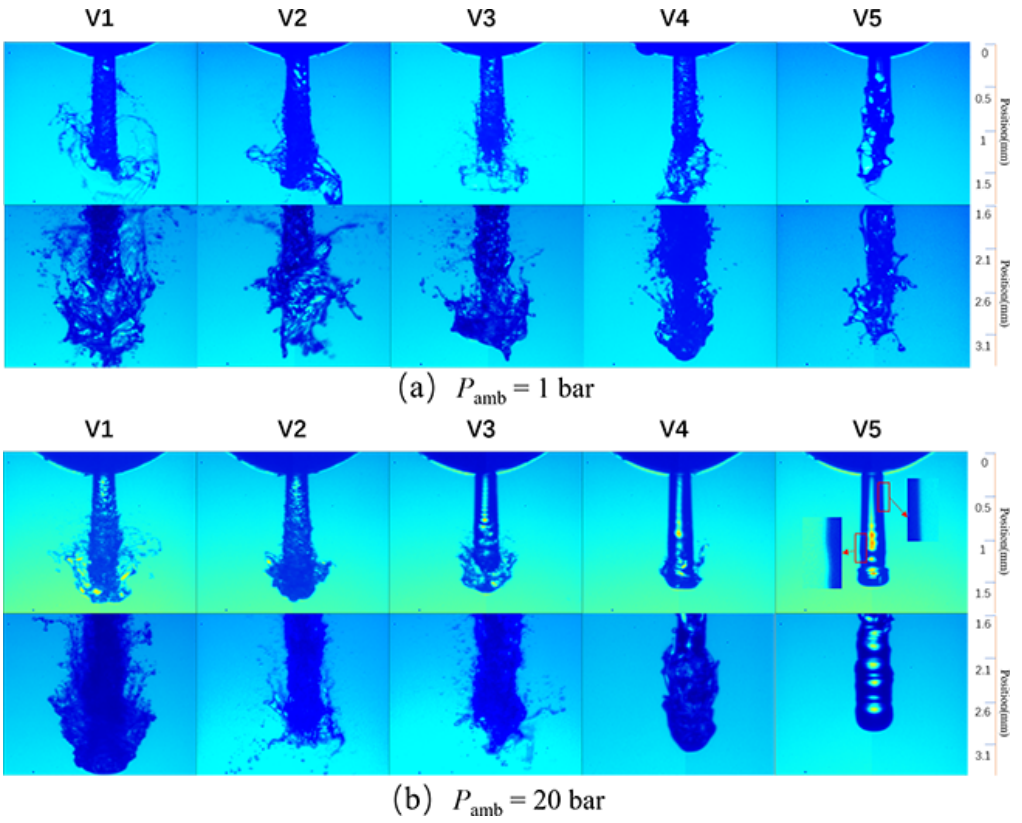

FIG. 8: Comparison of spray microscopic morphology at near-nozzle region between different viscosity liquids

is induced by two mechanisms. For more viscous liquid, the velocity of the flow will be reduced, as evidenced by the spray tip velocity shown in Fig. 9(a). This may be because of more pressure loss inside the nozzle. It is supposed that in spite of high lubricity, which should reduce friction in the nozzle (Hwang et al., 2017), the higher viscosity appeared to have a dominant effect on viscous resistance to the needle motion in the nozzle. Desantes et al. (2009) found that the movement of the needle for biodiesel will take more time compared with diesel, and the result is a longer time for the injector to get totally open. They also attributed it to the high viscosity of biodiesel, which is stickier, so the needle will not work as it does with regular diesel. This slower velocity then increases the cavitation number and inhibits the liquid sheet-like breakup caused by bubble bursting. As a consequence, no liquid sheet-like breakup was observed for more viscose liquids (V4 and V5). Additionally, the higher viscosity liquids significantly reduce the flow Reynolds number by increasing the kinematic viscosity and reducing the flow velocity. Previous work (Hwang et al., 2017) demonstrated that the effects of turbulence are quite significant for the wave growth and breakup of the jet. As a consequence, higher viscosity liquids lead to less jet breakup as observed in the images in Fig. 8(a).

For high ambient pressure cases (P_{amb} = 20 bar), which have a lower nozzle hole flow velocity compared to P_{amb} = 1 bar case for given fluids as shown in Fig. 8(b), the jet surface becomes smoother with the increase of viscosity, as shown in the first row. For V1 and V2,

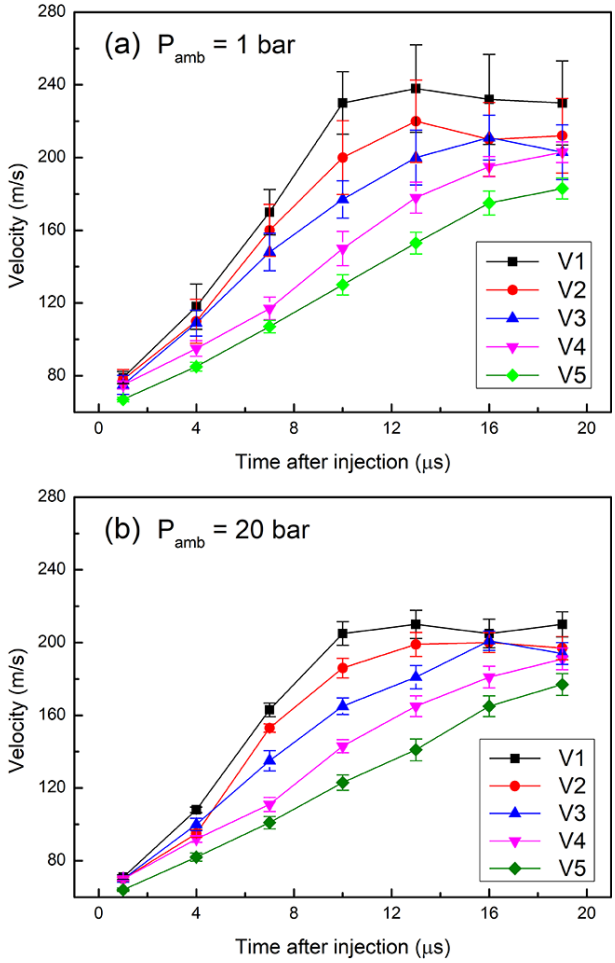

FIG. 9: Effect of viscosity on near-nozzle spray tip velocity

the surface wave is still unstable and some ligaments and small droplets are formed. With the increase of viscosity, the primary breakup is progressively inhibited. As the spray evolved, for V1, V2, and V3, ligaments and droplets are formed and exfoliated from the jet column and tip, though the quantity becomes less for V2 and V3. Few ligaments are formed for V4, and primary breakup for V5 is totally inhibited since only a jet column with a large scale of surface wave was observed. This is also caused by both the reduced cavitation and turbulence influence through reduced flow velocity, as evidenced by Fig. 9(b).

3.2 Macroscopic Spray Tip Penetration

The high-speed–camera-recorded macroscopic images were processed, and the contour of the spray can be extracted. Figure 10 presents the typical spray contour and the STP is defined as the distance between the farthest point of the spray and the nozzle exit. The experiments were repeated four times for each condition, and all the experimental data is shown in the figures.

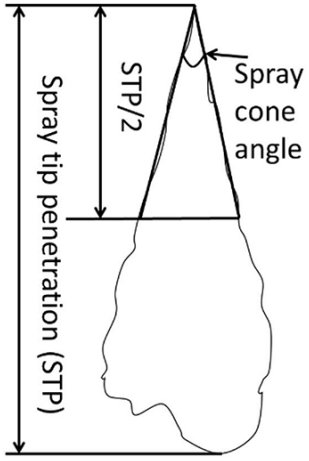

FIG. 10: Definition of spray tip penetration and spray cone angle

3.2.1 Effect of Surface Tension

STPs for different surface tension liquids were profiled as a function of time (t) at three ambient pressures, as shown in Fig. 11. The zero time is defined as the instant for the first appearance of liquid jet from the nozzle tip. Figure 11(a) shows that at $P_{amb} = 1$ bar, the STP for all the liquids grow quasi-linearly with t. In addition, the STP evolutions for different liquids remain almost the same. This is because the air entrainment effect is not obvious when the air density is low; the surface tension has little effect on the whole spray tip evolution at atmospheric pressure. At high ambient pressures, as shown in Figs. 11(b) and 11(c), at the early stage of the injection all liquids have similar STP, and the STP increases linearly. However, the growth rate decreases after a period of time and the STP for liquids with different surface tension becomes noticeable and the difference increases as the spray evolves. This may be explained as follows. In the second breakup process, ligaments and big droplets break up into small droplets under aerodynamic forces. In the research of Davanlou et al. (2015), the results showed that surface tension as the resistance to deformation hinders the breakup process. An increase in surface tension leads to a larger droplet diameter, so larger droplets with high inertia at the spray tip are more difficult to be entrained by the ambient air. This phenomenon was also found in the near-nozzle spray. Therefore, less momentum is transferred to the entrained gas resulting in longer STP.

3.2.2 Effect of Viscosity

Figure 12 provides the comparison of STP evolution for liquids with different viscosity at $P_{amb} = 1$, 10, and 20 bar. Similarly, the STP of all the liquids grow linearly with t and show little difference at $P_{amb} = 1$ bar. At $P_{amb} = 10$ and 20 bar, at the early stage of the injection all liquids have similar STP, and the STP increases linearly with t. In addition, the tip velocity become smaller as liquid viscosity increased at all ambient pressures in the near-nozzle region. There is a significant increase of STP with the increase of viscosity. This is because liquid with higher viscosity delays the primary breakup by suppressing the instabilities caused by the turbulence and cavitation, as discussed in Section 3.1. As a result, the second breakup is retarded, which in return increases the liquid inertia of the spray, resulting in increased STP.

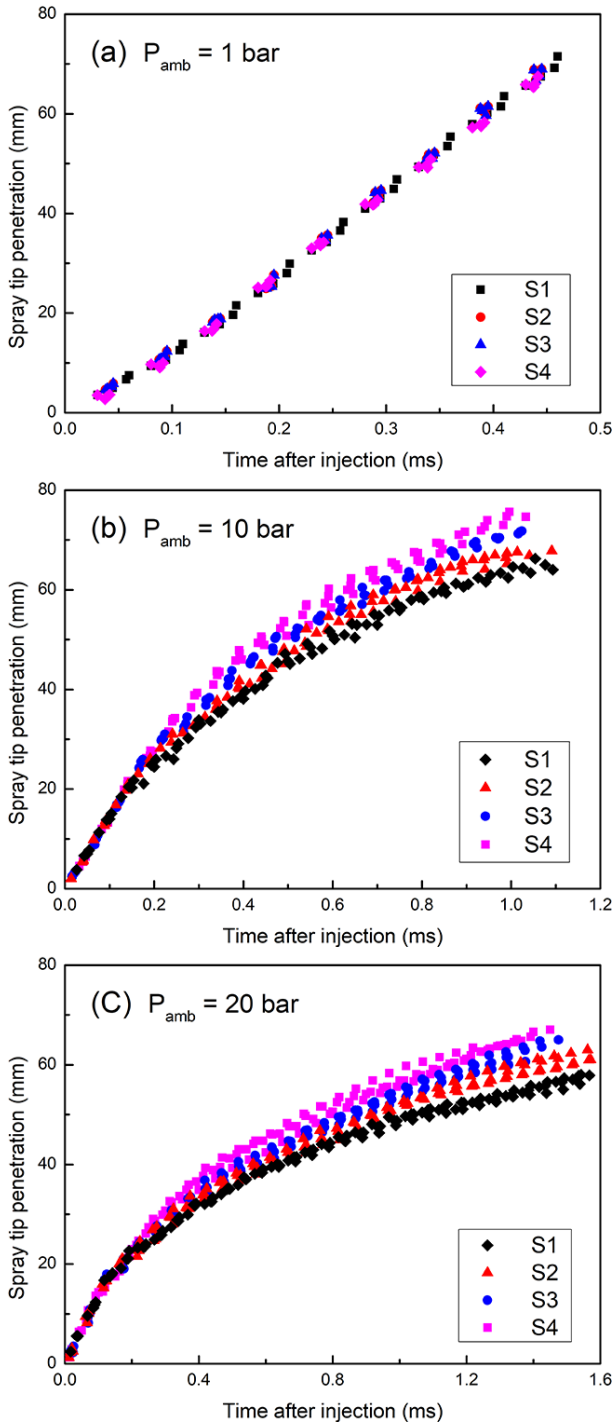

FIG. 11: Macroscopic STP evolution for different surface tension liquids

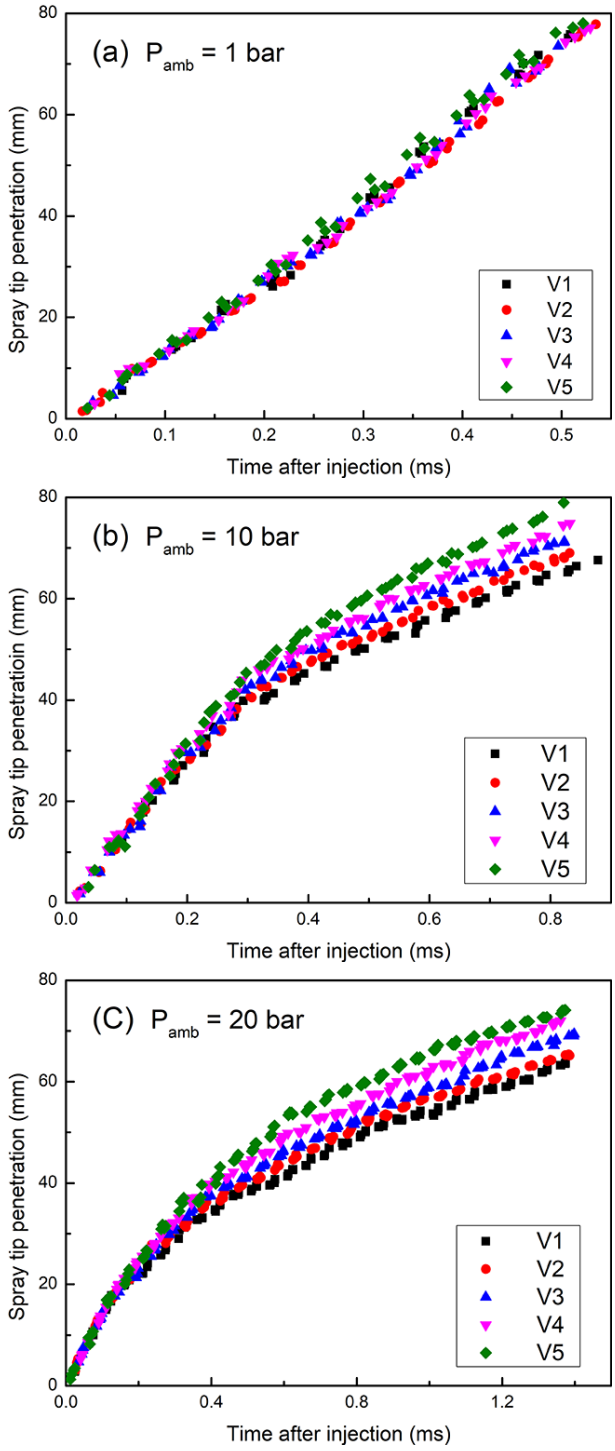

FIG. 12: Macroscopic STP evolution for different viscosity liquids

3.2.3 Empirical Model for Spray Tip Penetration

The above results have shown that both increasing the surface tension and viscosity increase the STP. Previously, several empirical models for STP (Hiroyasu and Arai, 1990; Kegl and Lešnik, 2018; Payri et al., 2005, 2007) have been developed based on experimental results and also have been extrapolated to predict the data that are difficult to be collected experimentally. Specifically, Hiroyasu and Arai (1990) correlated the STP as a function of time,

$$t < t_{break}: \quad \text{STP} = 0.39 \cdot \left(\frac{2\Delta p}{\rho_l}\right)^{0.5} \cdot t \tag{2}$$

$$t > t_{break}: \quad \text{STP} = 2.95 \cdot \left(\frac{\Delta p}{\rho_g}\right)^{0.25} \cdot (D \cdot t)^{0.5} \tag{3}$$

$$t_{break} = \frac{28.65 \cdot \rho_l D}{(\rho_g \Delta p)^{0.5}} \tag{4}$$

where STP is the STP (m), t is the time (s), ΔP is the pressure difference between the injection and ambient pressure (Pa), ρ_l and ρ_g are the liquid fuel and ambient gas density (kg/m^3), respectively, and D is the nozzle hole diameter (m). t_{break} is the breakup time before and after which the STP grows linearly and in square root with t. At the start of the injection, the fuel density and injection pressure dominate the spray penetration, after which the air entrainment process in the chamber becomes more dominant. This empirical equation was derived from summarizing experimental results concerning diesel fuel sprays. However, the other fuels with different physical properties, especially surface tension and viscosity, which also have significant effect on the STP, were not considered in this equation. So, we will provide a modified correlation to accommodate the viscosity and surface tension effect for the STP.

The comparison of the empirical model and the experimental data of each liquid is illustrated in Figs. 13 and 14. Specially, the data at $P_{amb} = 1$ bar is not concluded, as all the data are at the stage before breakup, and little difference was found. In the figures, the breakup time of the Hiroyasu model is labeled. In the Hiroyasu model, the straight slope seems a little different with

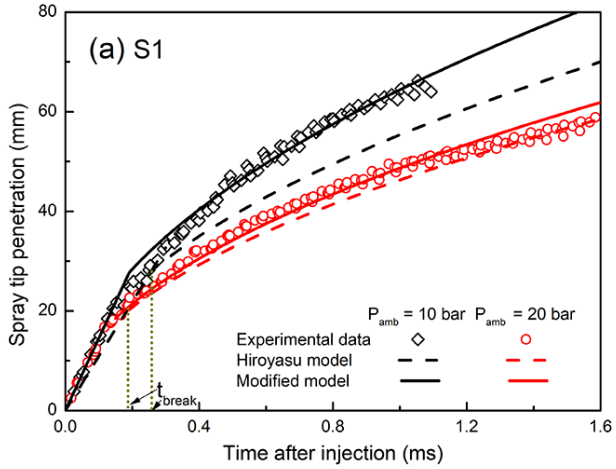

FIG. 13.

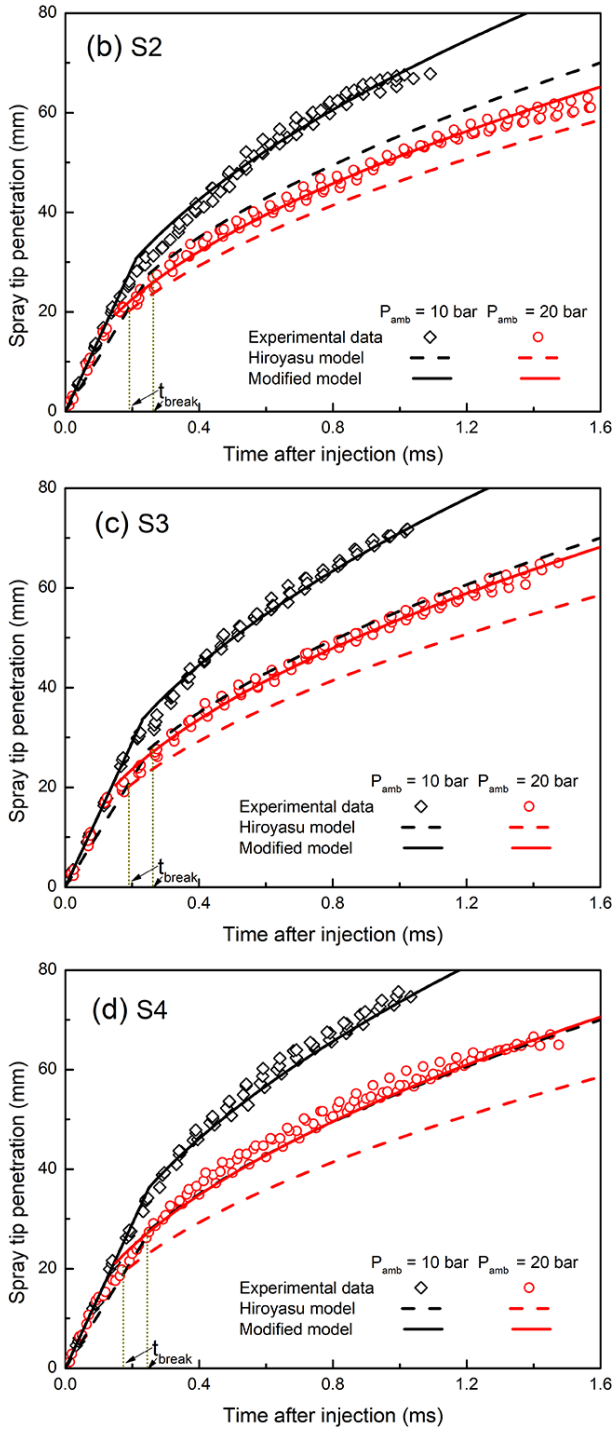

FIG. 13: STP experimental data, Hiroyasu model, and modified model for different surface tension liquids

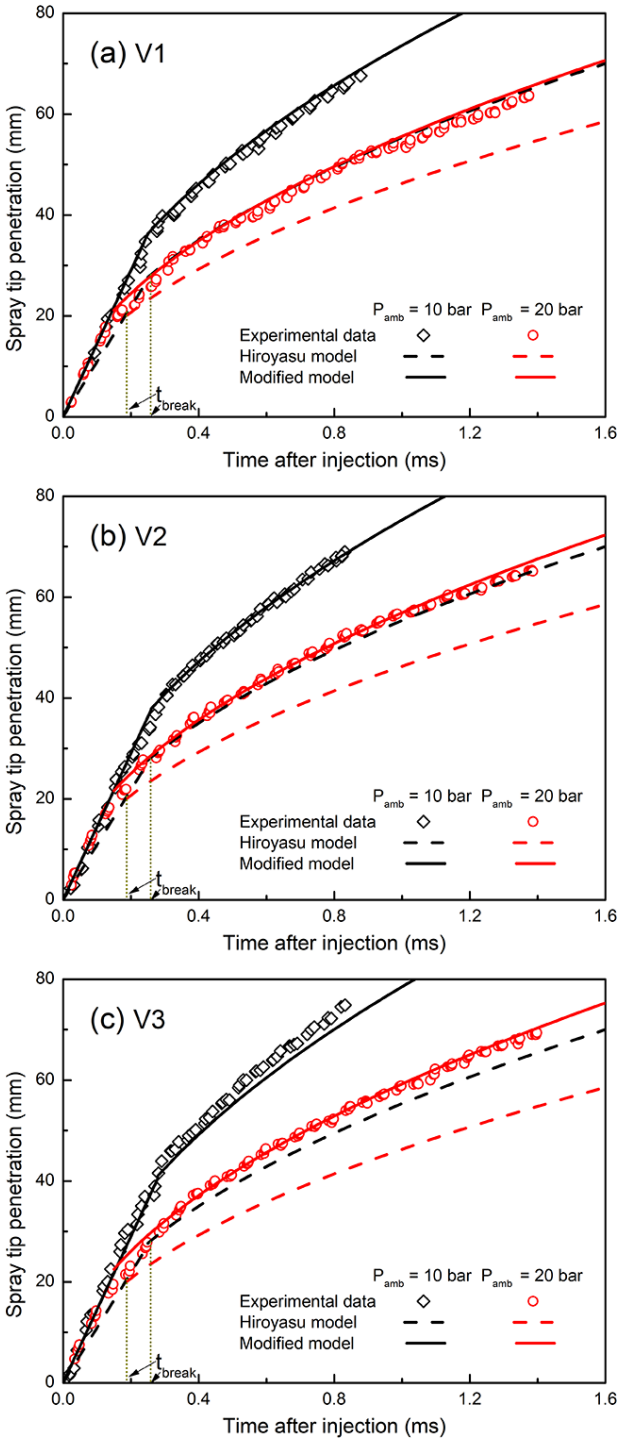
(a) V1
(b) V2
(c) V3
Spray tip penetration (mm)
Time after injection (ms)
0
20
40
60
80
0.0
0.4
0.8
1.2
1.6
P_{amb} = 10 bar P_{amb} = 20 bar
Experimental data
Hiroyasu model
Modified model
t_{break}

FIG. 14.

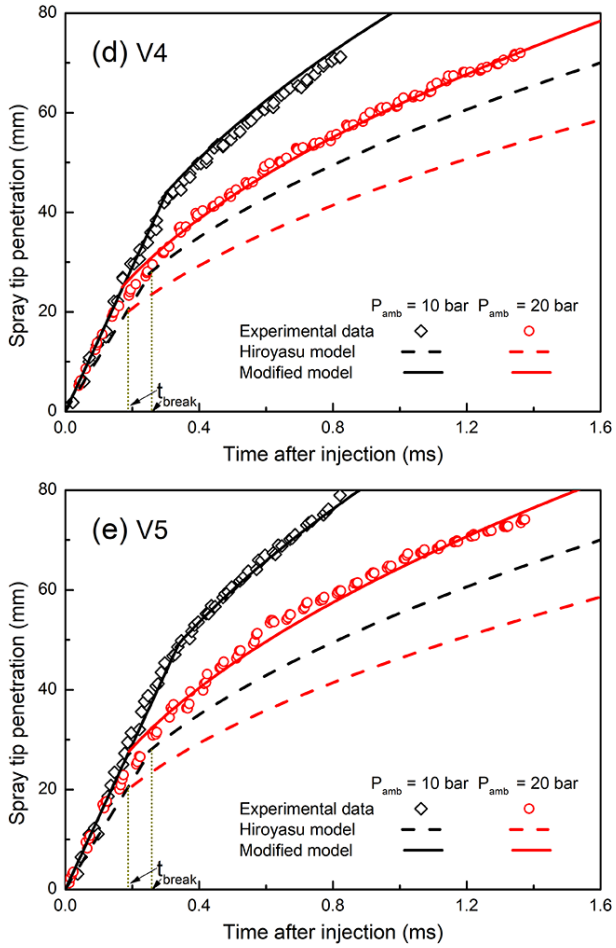

FIG. 14: STP experimental data, Hiroyasu model, and modified model for different viscosity liquids

our data before breakup time, although the difference is independent on ambient pressure, surface tension, and viscosity. This is because although Hiroyasu and Arai have taken the pressure differential and fuel density into account, the difference may also be attributed to the injector structure, fuel supply system, and optical path setup. Using a new absolute term, Eq. (2) can be rewritten as

$$\mathrm{STP} = a\left(\frac{2\Delta P}{\rho_l}\right)^{0.5} t \tag{5}$$

The fitting result shows that the value of a is 0.52. The correlation coefficient (R^2) is 0.995, indicating the robustness of Eq. (5) fitting. We note that a may influence other parameters such as injector type or nozzle structure.

For the root function after breakup time, the difference between the experimental data and the theoretical correlation is more obvious. In previous studies, other parameters that the Hiroyasu model did not consider such as fuel density and nozzle structure were proved to have the influence of STP (Bohl et al., 2017; Tang et al., 2017a). According to our experimental data, it

seems likely that the surface tension and viscosity also have significant influence on the STP. We then attempted to extend Eq. (3) to accommodate the effect of surface tension (S) and viscosity (V) on the STP evolution. For $P_{inj} \gg P_{amb}$, the variation of ΔP is negligible, and new equations are written as follows:

$$\mathrm{STP} = b\rho_g^{b_1} S^{b_2} V^{b_3} t^{b_4} \tag{6}$$

where the value for b is constant for all liquid types, as ΔP and D do not change when changing experimental conditions. After rearranging and linearizing the equation, we can write it as

$$ln^{\mathrm{STP}} = ln^b + b_1 ln^{\rho_g} + b_2 ln^S + b_3 ln^V + b_4 ln^t \tag{7}$$

By applying the least-square fitting method, all four times repeating experimental data of the tested liquids were used to fit Eq. (7). The values and corresponding standard error are shown in Table 2.

The new and modified STP equation can now be written as

$$\mathrm{STP} = 3.27\Delta P^{0.25} D^{0.5} \rho_g^{-0.406} S^{0.158} V^{0.074} t^{0.5} \tag{8}$$

The R^2 of the fitting result is 0.984. In addition, the modified STP correlation has been plotted in Figs. 13 and 14 for all the liquids at $P_{amb} = 10$ and 20 bar. It can be concluded that the modified correlation matches the experimental data very well for different types of liquids with changing surface tension and viscosity. Here, it should be noted that the constant term in the equations may also contain influence of other parameters such as nozzle structure and fuel density. Specially, the power law of S and V are 0.158 and 0.074, respectively. It is indicated that the surface tension has a more distinct influence on STP evolution after breakup time. However, we note that the effect of these two factors on STP evolution is weak, compared to other factors such as injection pressure and air density.

The decreased STP is attributed to the decrease of spray droplet size, which will increase the aerodynamic drag force, decrease spray momentum, and eventually slow down the penetration as much research discussed (Bohl et al., 2017; Feng et al., 2016; Kegl and Lešnik, 2018). So, we inferred that the surface tension has a more distinct effect on the second breakup than viscosity. The SMD model correlation of Elkotb (1982) was presented in terms of dynamic viscosity and surface tension of the injected fuel as

$$\mathrm{SMD} = 6156\Delta P^{-0.54} \rho_g^{0.06} \rho_f^{0.352} V^{0.385} S^{0.737}\ \mu\mathrm{m} \tag{9}$$

It is suggested that the SMD is proportional to surface tension and viscosity and the effect of surface tension is a little bit more obvious for the power law of S and V, which are 0.737 and 0.385, respectively. It is consistent with our inference. However, there are also some limitations to the SMD correlations, so in our next work, these liquids will be used in the SMD measurement.

TABLE 2: New correlation factors for modified model

Parameters	**b**	**b_1**	**b_2**	**b_3**	**b_4**
Fitting value	3.630	–0.406	0.158	0.074	0.500
Standard error	0.021	0.003	0.003	0.001	0.002
$R^2 = 0.984$					

3.3 Macroscopic Spray Cone Angle

The SCA is defined as the angle covered by the two tangent lines, which connects the nozzle tip and the periphery points at the position of STP/2, as shown in Fig. 10. The transient changes of SCA for each liquid at $P_{amb} = 10$ bar are shown in Fig. 15. The SCAs experience a rapid decrease during the early stage and after about 0.1 ms, SCA becomes almost a constant because the injection experiences a steady state period with the nozzle hole holding full open. The empirical equation of the Hiroyasu model for SCA when this angle reaches the constant value is expressed by the following:

$$\mathrm{SCA} = 83.5 \left(\frac{L}{D}\right)^{-0.22} \left(\frac{D}{D_s}\right)^{0.15} \left(\frac{\rho_g}{\rho_f}\right)^{0.26} \tag{10}$$

where D_s is the sack chamber diameter of the nozzle. It is observed that the SCAs of the text liquids are smaller than that of the Hiroyasu model, which is attributed to the increased viscosity

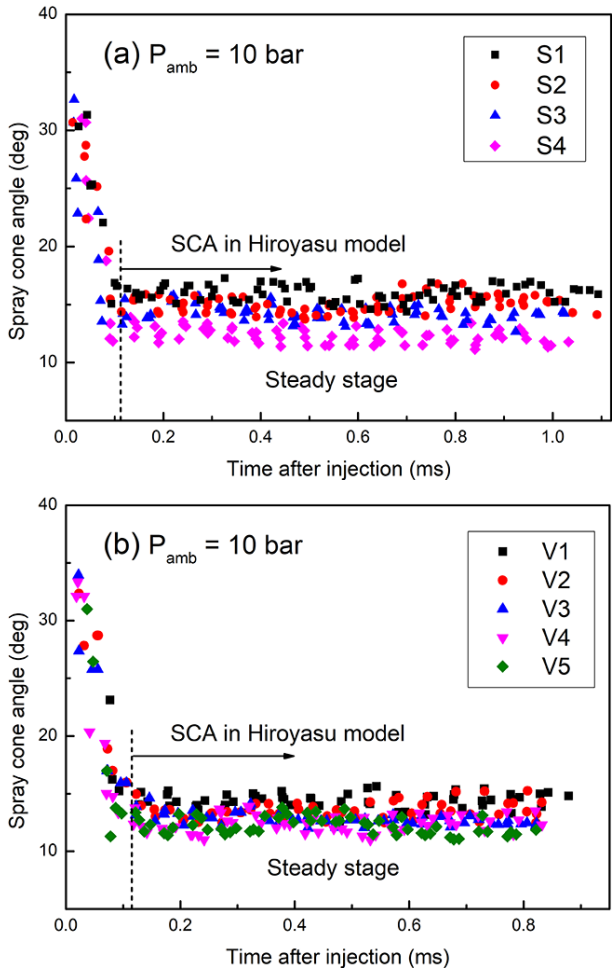

FIG. 15: Spray cone angle evolution of tested liquids at $P_{amb} = 10$ bar

and surface tension of the liquids. We also note that the fluctuations of SCA at the steady stage are mainly a result of perturbation of the spray periphery due to the gas entrainment. As such, the SCAs at the steady state stage are averaged.

The average SCA as a function of surface tension and viscosity is presented in Fig. 16. The error bars represent the standard deviation in the four repeated experiments. At $P_{amb} = 1$ bar, the SCA for different surface tension and viscosity liquids shows little difference. However, at higher ambient pressures, the SCA becomes smaller with the increase of liquid surface tension as shown in Fig. 16(a). This may be attributed to the smaller droplet size in low surface tension sprays at the same spatial location, which leads to significant centrifugal dispersion due to lower inertia causing a wider SCA.

With the increase of viscosity at $P_{amb} = 10$ and 20 bar, as shown in Fig. 16(b), the average SCA first decreases and then gradually becomes a constant. This is consistent with the observations of Hwang et al. (2016), in which they showed that the lower level of turbulence in the spray boundary leading to a more stable structure would result in reduced diffusion of the spray in the

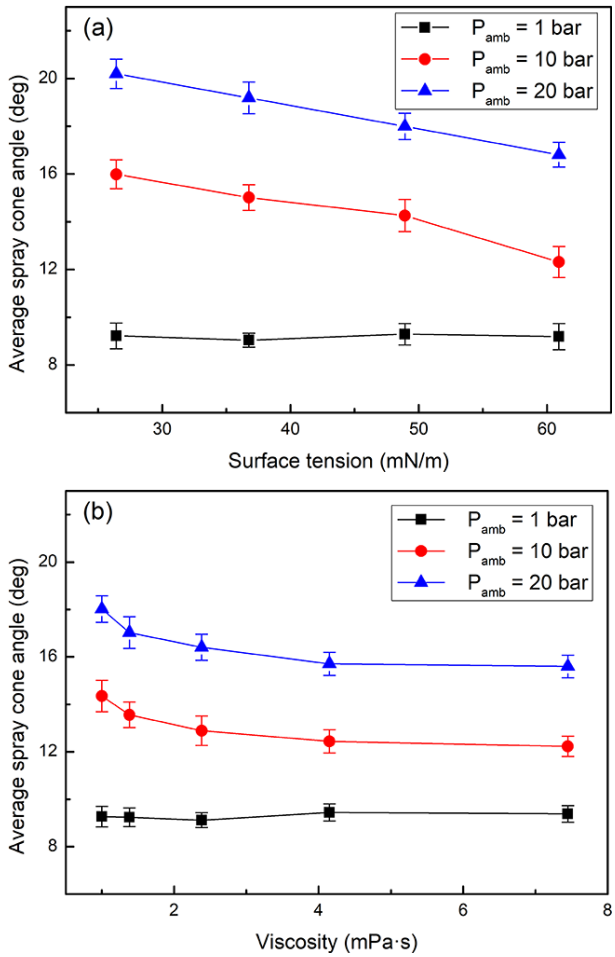

FIG. 16: Average SCA for different ambient pressures as a function of (a) surface tension and (b) viscosity

radial direction. As a consequence, increased viscosity with reduced level of turbulence finally results in smaller SCA. However, the viscosity effect may finally reach its limit, as shown that the decreased rate of SCA becomes smaller with the increase of viscosity, and little difference is found between V4 and V5.

We further compared the effect of surface tension and viscosity on the average SCA at 10 and 20 bar ambient pressures, as shown in Fig. 17. It demonstrates the sensitivity of average SCA to surface tension and viscosity. The top and bottom horizontal axle represent, respectively, the ratio of the surface tension and viscosity to the reference surface tension and viscosity. At first, increasing the surface tension by 50% yields a similar percentage of SCA change as increasing viscosity by 50%, indicating that the SCA shows quantitatively similar dependence on the surface tension and viscosity. Then at a higher ratio, surface tension becomes more effective in reducing the SCA compared to the viscosity.

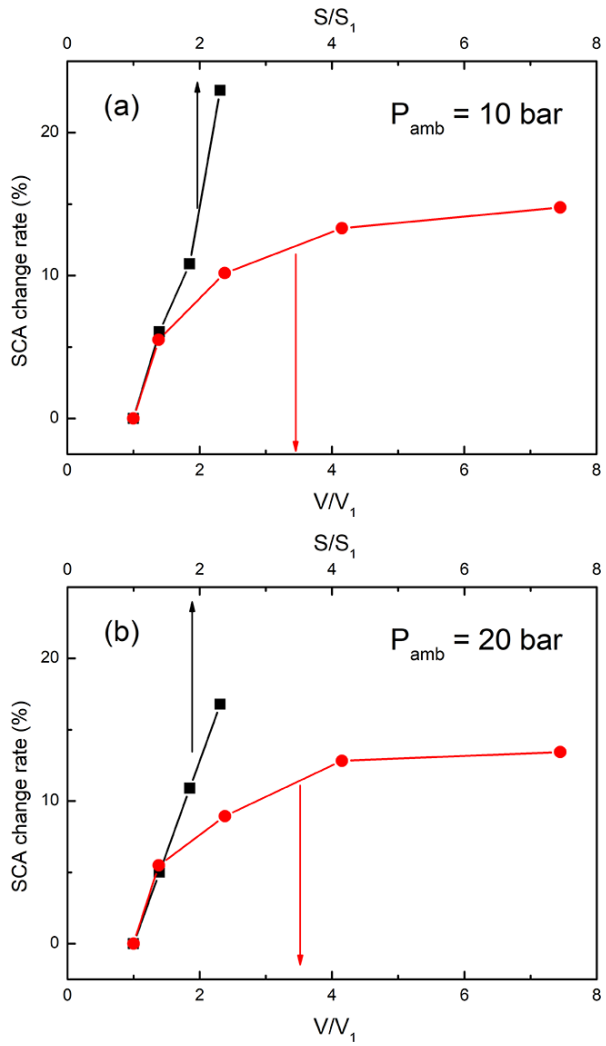

FIG. 17: Comparison of the average SCA sensitivity to surface tension and viscosity

4. CONCLUSIONS

In this work, experimental investigations on the individual effect of liquid surface tension and viscosity on the spray characteristics have been conducted at different ambient pressures using a single-hole diesel injector. The near-nozzle spray morphology and the macroscopic characteristics such as STP and SCA for all the tested liquids have been obtained. Results show that,

1. Under the effect of aerodynamics forces, many thread-like ligaments and small droplets are created at the crest of the surface wave and liquid film at the edge of the jet tip in the near-nozzle region at high ambient pressures. Catastrophic breakup caused by the cavitation was commonly observed under atmospheric pressure. Both cases will promote primary breakup. With the increase of liquid surface tension, the liquid sheet-like structures are observed under atmospheric pressure. Slightly less ligaments and droplets are detected with the increase of surface tension at high ambient pressures. Compared to the surface tension, the near-nozzle spray morphology is more sensitive to the variation of viscosity; more stable structures and lower spray-tip velocity were observed with the increase of viscosity. The elevated viscosity dampens the deformation of the liquid, which leads to a delayed liquid breakup and consequently postpones the formation of spray ligaments and droplets.

2. Under the atmospheric pressure, the macroscopic STP and SCA of all the tested liquids show little difference. However, the STP becomes larger with the increase of surface tension or viscosity. The Hiroyasu model for STP after the breakup time is extended to account for the effect of the surface tension and the viscosity. The modified empirical model yields good performance on STP evolution prediction. The results also indicate that surface tension has a more distinct influence on STP evolution after breakup time compared with viscosity.

3. The average SCA becomes smaller with the increase of liquid surface tension, and first decreases then gradually becomes a constant with the increase of viscosity at high ambient pressures. The SCA shows quantitatively similar dependence on the surface tension and viscosity, when the two parameters increase by 50%, respectively. However, surface tension becomes more effective in reducing the SCA, compared to the viscosity.

ACKNOWLEDGMENTS

This work at Xi'an Jiaotong University was supported by the National Natural Science Foundation of China (Nos. 51722603, 91941101) and the Open Research Fund of Beijing Key Laboratory of Powertrain for New Energy Vehicle, Beijing Jiaotong University. CT is a Tang Scholar and we acknowledge China Scholarship Council (CSC) for the funding support. The support from Department of Mechanical System Engineering, University of Hiroshima is also acknowledged.

REFERENCES

Agarwal, A.K., Dhar, A., Gupta, J.G., Kim, W.I., Lee, C.S., and Park, S., Effect of Fuel Injection Pressure and Injection Timing on Spray Characteristics and Particulate Size–Number Distribution in a Biodiesel Fuelled Common Rail Direct Injection Diesel Engine, *Appl. Energy*, vol. **130**, pp. 212–221, 2015.

Bohl, T., Tian, G., Smallbone, A., and Roskilly, A.P., Macroscopic Spray Characteristics of Next-Generation Bio-Derived Diesel Fuels in Comparison to Mineral Diesel, *Appl. Energy*, vol. **186**, pp. 562–573, 2017.

Chung, I.P. and Presser, C., Fluid Property Effects on Sheet Disintegration of a Simplex Pressure-Swirl Atomizer, *J. Propul Power*, vol. **17**, no. 1, pp. 212–216, 2001.

Davanlou, A., Lee, J.D., Basu, S., and Kumar, R., Effect of Viscosity and Surface Tension on Breakup and Coalescence of Bicomponent Sprays, *Chem. Eng. Sci.*, vol. **131**, pp. 243–255, 2015.

Desantes, J.M., García-Oliver, J.M., Xuan, T., and Vera-Tudela, W., A Study on Tip Penetration Velocity and Radial Expansion of Reacting Diesel Sprays with Different Fuels, *Fuel*, vol. **207**, pp. 323–335, 2017.

Desantes, J.M., Payri, R., García, A.G., and Manin, J., Experimental Study of Biodiesel Blends Effects on Diesel Injection Processes, *Energy Fuels*, vol. **23**, pp. 3227–3235, 2009.

Elkotb, M.M., Fuel Atomization for Spray Modelling, *Pro. Energy Combust. Sci.*, vol. **8**, pp. 61–91, 1982.

Ellis, M.C.B., Tuck, C.R., and Miller, P.C.H., How Surface Tension of Surfactant Solutions Influences the Characteristics of Sprays Produced by Hydraulic Nozzles Used for Pesticide Application, *Colloids Surf.*, vol. **180**, pp. 267–276, 2001.

Feng, Z., Zhan, C., Tang, C., Yang, K., and Huang, Z., Experimental Investigation on Spray and Atomization Characteristics of Diesel/Gasoline/Ethanol Blends in High Pressure Common Rail Injection System, *Energy*, vol. **112**, pp. 549–561, 2016.

Hiroyasu, H. and Arai, M., Structures of Fuel Sprays in Diesel Engines, SAE paper 900475, 1990.

Hwang, J., Bae, C., and Gupta, T., Application of Waste Cooking Oil (WCO) Biodiesel in a Compression Ignition Engine, *Fuel*, vol. **176**, pp. 20–31, 2016.

Hwang, J., Bae, C., Patel, C., Agarwal, A.K., and Gupta, T., Near Nozzle Flow and Atomization Characteristics of Biodiesel Fuels, *SAE International*, 2017-01-2327.

Kegl, B. and Lešnik, L., Modeling of Macroscopic Mineral Diesel and Biodiesel Spray Characteristics, *Fuel*, vol. **222**, pp. 810–820, 2018.

Kowalski, J., The Theoretical Investigation on Influence the Fuel Spray Geometry on the Combustion and Emission Characteristic of the Marine Diesel Engine, *Combust. Engines*, vol. **169**, no. 2, pp. 101–107, 2017.

Li, F., Yi, B., Fu, W., Song, L., Liu, T., Hu, H., and Lin, Q., Experimental Study on Spray Characteristics of Long-Chain Alcohol-Diesel Fuels in a Constant Volume Chamber, *J. Energy Inst.*, vol. **112**, 2017.

Mohan, B., Yang, W., Yu, W., and Tay, K.L., Numerical Analysis of Spray Characteristics of Dimethyl Ether and Diethyl Ether Fuel, *Appl. Energy*, vol. **185**, pp. 1403–1410, 2017.

Moon, S., Gao, Y., Wang, J., Fezzaa, K., and Tsujimura, T., Near-Field Dynamics of High-Speed Diesel Sprays: Effects of Orifice Inlet Geometry and Injection Pressure, *Fuel*, vol. **133**, pp. 299–309, 2014.

Payri, R., Ruiz, S., Salvador, F.J., and Gimeno, J., On the Dependence of Spray Momentum Flux in Spray Penetration: Momentum Flux Packets Penetration Model, *J. Mech. Sci. Technol.*, vol. **21**, pp. 1100–1111, 2007.

Payri, R., Salvador, F.J., Gimemo, J., and Soare, V., Determination of Diesel Sprays Characteristics in Real Engine In-Cylinder Air Density and Pressure Conditions, *J. Mech. Sci. Technol.*, vol. **19**, no. 11, pp. 2040–2052, 2005.

Ramamurthi, K., Tharakan, T.J., and Balakrishnan, M., Flow Transition in Swirled Liquid Sheets, *AIAA J.*, vol. **36**, no. 3, pp. 420–427, 1998.

Sallevelt, J.L.H.P., Pozarlik, A.K., and Brem, G., Characterization of Viscous Biofuel Sprays Using Digital Imaging in the near Field Region, *Appl. Energy*, vol. **147**, pp. 161–175, 2015.

Shinjo, J. and Umemura, A., Simulation of Liquid Jet Primary Breakup: Dynamics of Ligament and Droplet Formation, *Int. J. Multiphase Flow*, vol. **36**, pp. 513–532, 2010.

Som, S. and Aggarwal, S.K., Effects of Primary Breakup Modeling on Spray and Combustion Characteristics of Compression Ignition Engines, *Combust. Flame*, vol. **157**, no. 6, pp. 1179–1193, 2010.

Suh, H.K. and Lee, C.S., Effect of Cavitation in Nozzle Orifice on the Diesel Fuel Atomization Characteristics, *Int. J. Heat Fluid Flow*, vol. **29**, no. 4, pp. 1001–1009, 2008.

Tang, C., Feng, Z., Zhan, C., Ma, W., and Huang, Z., Experimental Study on the Effect of Injector Nozzle K Factor on the Spray Characteristics in a Constant Volume Chamber: Near Nozzle Spray Initiation, the Macroscopic and the Droplet Statistics, *Fuel*, vol. **202**, pp. 583–594, 2017.

Tang, C., Guan, L., Feng, Z., Zhan, C., Yang, K., and Huang, Z., Effect of Di-n-Butyl Ether Blending with Soybean-Biodiesel on the Near-Nozzle Spray Characteristics, *Fuel*, vol. **191**, pp. 300–311, 2017.

Wang, X., Huang, Z., Kuti, O.A., Zhang, W., Nishida, K., Experimental and Analytical Study on Biodiesel and Diesel Spray Characteristics under Ultra-High Injection Pressure, *Int. J. Heat Fluid Flow*, vol. **31**, pp. 659–666, 2010.

Wang, Z., Ding, H., Ma, X., Xu, H., and Wyszynski, M.L., Ultra-High Speed Imaging Study of the Diesel Spray Close to the Injector Tip at the Initial Opening Stage with Single Injection, *Appl. Energy*, vol. **165**, pp. 335–344, 2016.

Wang, Z., Ding, H., Ma, X., Xu, H., and Wyszynski, M.L., Ultra-High Speed Imaging Study of the Diesel Spray Close to the Injector Tip at the Initial Opening Stage with Split Injection, *Appl. Energy*, vol. **163**, pp. 105–117, 2016.

Wei, M., Gao, Y., Yan, F., Chen, L., Feng, L., Li, G., and Zhang, C., Experimental Study of Cavitation Formation and Primary Breakup for a Biodiesel Surrogate Fuel (Methyl Butanoate) Using Transparent Nozzle, *Fuel*, vol. **203**, pp. 690–699, 2017.

Yao, S., Zhang, J., and Fang, T., Effect of Viscosities on Structure and Instability of Sprays from a Swirl Atomizer, *Exp. Therm. Fluid Sci.*, vol. **39**, pp. 158–166, 2016.

Yu, W., Yang, W., Mohan, B., Tay, K.L., and Zhao, F., Macroscopic Spray Characteristics of Wide Distillation Fuel (WDF), *Appl. Energy*, vol. **185**, pp. 1372–1382, 2017.

Yu, Y., Li, G., Wang, Y., and Ding, J., Modeling the Atomization of High-Pressure Fuel Spray by Using a New Breakup Model, *Appl. Math. Model.*, vol. **40**, no. 1, pp. 268–283, 2016.

Zhan, C., Feng, Z., Ma, W.A., Zhang, M., Tang, C., and Huang, Z., Experimental Investigation on Effect of Ethanol and Di-Ethyl Ether Addition on the Spray Characteristics of Diesel/Biodiesel Blends under High Injection Pressure, *Fuel*, vol. **218**, pp. 1–11, 2018.